KRONOS FUSION ENERGY

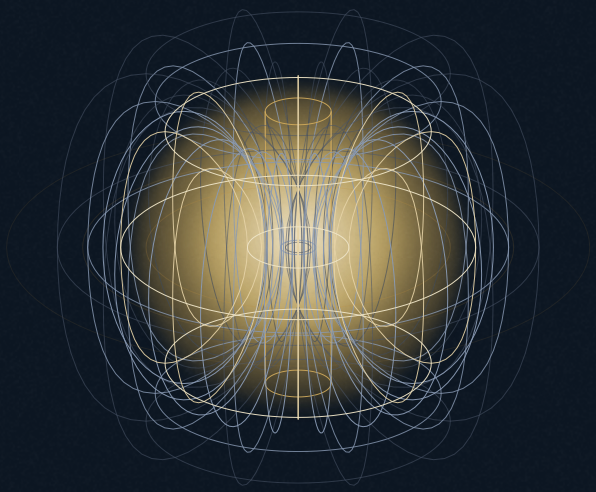

PAPER 2.39 · THE KRONOS 2026 SERIES

A Flowing-Lithium Vapor-Box Divertor with Molten-Salt In-Loop Tritium Extraction for a Compact Spherical-Tokamak Breeder

A compact spherical tokamak concentrates its exhaust power onto a small divertor and, in a nuclear device, onto a surface that must not become a tritium reservoir. A solid target…

Read it live — 3-D model · physics validator · film series

BY P I FORD AND G L KULCINSKI

2026 · EDITORIAL EDITION

THE OFFICIAL RECORD

What this document is, and how to read its numbers

This is a combined editorial. It gathers, in one volume, the two design studies Kronos Fusion Energy released in 2026 — a compact spherical-tokamak tritium/helium-3 breeder and a deuterium–helium-3 tandem-mirror generator — together with the intellectual-property estate, the people, and, in the internal edition, the full commercial case. The scientific text is the same text that appears in the arXiv preprints and the journal submissions; the editorial adds the apparatus a reader needs to hold the whole program at once, and nothing in the physics is altered to fit it.

THE HONESTY STANCE IS THE ASSET

Every headline quantity carries an **evidence class** — DERIVED · RECOMPUTED · MEASURED · REQUIREMENT — and, where a number is a modelled extrapolation rather than a demonstrated value, it is labelled as such and its downside is shown next to it. Several quantities in the underlying corpus moved after first publication; where a value has been withdrawn or restated, the record says so plainly. This is deliberate: a diligence team will find the load-bearing assumptions, so the document surfaces them first.

TWO EDITIONS

This volume is issued in two editions. The **public edition** (light) carries the physics and the design only — no dollar, price, or per-kilogram figure appears anywhere in it. The **internal edition** (dark) adds the economics, the funding architecture, and the defense-commercial analysis, and is marked *Confidential* accordingly; it is not for public distribution. Where the commercial case rests on a modelled assumption rather than a demonstrated one, it is labelled as such and its downside is shown alongside it, on the same terms as the physics.

TITLE	The Kronos Fleet — Hyperion · Aegis · MetroVolt: A Combined Design & Commercialization Study
AUTHOR	Priyanca Ford, Founder & CEO, on behalf of Kronos Fusion Energy
EDITION	2026 Combined Editorial · first issue
COMPANION WORKS	The five-paper arXiv drop — (1) Breeder, (2) Burner, (3) REBCO magnet & tape, (4) Direct Energy Conversion, (5) AI/ML/Quantum control — with matching numbered Zenodo deposits, plus the IOP journal and IAEA-FEC submissions. Patents were filed before the drop.
NAMING	Hyperion = the breeder; Aegis (defense) and MetroVolt (data-center) = one generator in two housings. Internal mode letters (D1, L) do not appear on public surfaces.
STATUS	Conceptual design & simulation study. Nothing herein is a construction commitment.

HOW TO READ THIS VOLUME

The fleet at a glance, and the way its numbers are marked

This volume opens with *Orientation*, presents the five research papers as a bound sequence, and closes with the *Apparatus*. *Foundations* sets out the three general results both machines rest on. *Paper One* is the Hyperion breeder; *Paper Two* the Aegis / MetroVolt generator; *Papers Three, Four and Five* are the enabling science — high-field REBCO magnets and tape, direct energy conversion, and the AI / ML / quantum control stack. A *Digital Twin & 3-D Model* part follows, then the *Environmental* profile. The *Economics* and levelized cost and the *Business Case* and diligence record appear in the internal edition only; the *Simulations* proof record and the Apparatus — patent portfolio, team, limitations, and sources — close both editions.

THE FLEET AT A GLANCE

	HYPERION	AEGIS	METROVOLT
Role	Strategic-isotope foundry	Defense installation power	Campus power
Machine	**Spherical tokamak**	**Tandem mirror**	**Tandem mirror**
Fuel	Deuterium–tritium	Deuterium–helium-3	Deuterium–helium-3
Delivers	Tritium · ^{3}He · 14 MeV n	Resilient installation power	Firm campus power
Physics bar	**Fusion gain only**	Closure (gates named)	Closure + lunar ^{3}He
In the fleet	Breeds the fuel	Proves the generator	Commercial destination

HOW THE NUMBERS ARE MARKED

Every headline quantity carries an evidence class — DERIVED from first principles, RECOMPUTED from raw data, MEASURED in hardware, or a REQUIREMENT yet to be met. Financial figures carry a case label and are confined to the internal (confidential) edition. Values that moved after first publication are shown as withdrawn or restated rather than quietly changed. A capability you can evaluate is one whose limits are on the page.

ABSTRACT

A Flowing-Lithium Vapor-Box Divertor with Molten-Salt In-Loop Tritium Extraction for a Compact Spherical-Tokamak Breeder

A compact spherical tokamak concentrates its exhaust power onto a small divertor and, in a nuclear device, onto a surface that must not become a tritium reservoir. A solid target erodes, thermally fatigues, and traps tritium; a flowing liquid-metal surface removes the first two failure modes by renewal, but the *choice* of metal is then set by tritium retention, because in a breeder the divertor is part of the fuel cycle. We formalise a flowing-lithium vapor-box divertor with molten-salt in-loop tritium extraction and reduce it to practice on the Hyperion breeder design point ($I_p = 9.66\,MA$, $Q = 3.076$, $P_{\mathrm{fus}} = 85.04\,MW$, negative triangularity $\delta = -0.30$, $B_0 = 8\,T$, elongation $\kappa = 2.0$, major radius $R_0 = 1.20\,m$, aspect ratio $A = 2.5$). We give the governing equations as a coupled system: the Hartmann-number magnetohydrodynamic drag on the film, the enthalpy- and evaporation-limited film heat balance $q_{\max} = \rho\, u\, \delta\, c_p\, \Delta T_{\mathrm{evap}}$, the two-point detachment model that sets the incident load, and the diffusion–trapping permeation problem whose Sieverts′-law solubility ordering explains the retention ranking. Coupled FESTIM/TMAP permeation–retention modelling at 673 K ranks four candidates by steady tritium loss relative to pure lithium: lithium $1\times$, a $Li_{62}Sn_{38}$ eutectic $6{,}812\times$, lead–lithium $41{,}889\times$, and pure tin $4{,}760{,}504\times$ — three to six orders of magnitude. Reduced thermofluid modelling gives a handled film heat flux of $2.8/4.9/6.7\,MW/m^2$ at film velocities of $2/5/10\,m/s$, and, in series with a stacked Super-X detached configuration, the vapor-box surface caps the peak target load from ~ 31 to $0.16\,MW/m^2$. In-loop molten-salt extraction converts what would be a static $\sim 1.3\,kg$ lithium tritium trap (37× the operating inventory) into a milligram-scale in-vessel inventory and a recovery stream. Flowing lithium therefore couples the two hardest subsystem problems — power handling and tritium inventory — into one solution. This is an internal-platform concept, not a built system; every headline number is a frozen anchor in the Kronos Physics De-Risking Register.

Open-access deposit (code & data, CC BY 4.0): DOI 10.5281/zenodo.22645750 · Zenodo community *kronos_fusion_energy*. Explore it live: interactive 3-D model · physics validator.

Keywords: liquid-metal divertor · flowing lithium · vapor box · tritium retention · molten-salt extraction · detachment · heat exhaust · spherical-tokamak breeder

CONTENTS

Table of Contents

NOMENCLATURE

Symbols, units, and the names of things

Q	plasma (fusion) gain, P_{fus}/P_{aux}
Q_E	engineering gain, net electric out / recirculating in
H_{98}	confinement enhancement over the IPB98(y,2) scaling
Z_{eff}	effective ion charge
c_{ee}	electron–electron bremsstrahlung leading coefficient, 2.120022 (exact)
τ_E	energy confinement time
I_p	plasma current
R_0, a	major radius, minor radius
κ, δ	elongation, triangularity
β_N	normalized plasma beta (Troyon-normalized)
TBR	tritium breeding ratio
DEC	direct energy conversion
CF	plant capacity factor (availability)
FOAK / NOAK / BOAK	first / n^{th} / best of a kind
Hyperion	the ST breeder (internal: Mode D2)
Aegis	the generator, defense/installation housing (internal: Mode M)
MetroVolt	the generator, data-center housing (Mode M)

liquid-metal divertor; flowing lithium; vapor box; tritium retention; molten-salt extraction; detachment; heat exhaust; spherical-tokamak breeder

§ 1

Introduction

THE EXHAUST PROBLEM OF A COMPACT BREEDER

The divertor is where a compact machine's power-handling problem is sharpest. A spherical tokamak (ST) confines a large plasma current in a small volume [1,2], which is precisely what makes it an attractive **14 MeV** neutron source and tritium-breeding platform and, at the same time, what concentrates the scrape-off-layer (SOL) power onto a divertor of only a few square metres. The same concentration challenge drives the compact, high-field tokamak line generally [25]. In the Hyperion breeder the parallel heat flux entering the SOL is of order $q_{\parallel} \sim 27\,GW/m^2$ into a heat-flux width of $\lambda_q \approx 0.21\,mm$ — consistent with the inverse-poloidal-field narrowing of the Eich multi-machine scaling [24,32]; without mitigation the peak load on a conventional attached target reaches $\sim 1.37\,GW/m^2$, two orders of magnitude above the $\sim 10\,MW/m^2$ that any actively cooled plasma-facing component (PFC) can steadily survive [3,4,5]. The power-exhaust problem is not incidental to the compact breeder; it is one of the two hardest constraints on whether the platform can be built at all.

Two families of solution exist and are complementary. The first shapes the magnetic geometry to spread and lengthen the exhaust channel — the Super-X [6], snowflake [7] and double-null configurations — and radiates the majority of the power volumetrically by impurity seeding before it reaches the target [8,9]. The second replaces the solid target itself with a renewable liquid metal, so that erosion and thermal fatigue are removed by continuous refreshing of the surface and the incident power is dissipated by evaporation and vapour-cloud radiation [11,12]. This paper is about the second family and, specifically, about which liquid metal a *breeder* must choose — a question whose answer is dictated not by thermal engineering but by tritium.

LIQUID-METAL PLASMA-FACING SURFACES AND THE VAPOR BOX

Liquid-metal PFCs have a mature experimental basis. Capillary-porous systems (CPS) that hold liquid lithium or tin against magnetohydrodynamic (MHD) ejection have run as limiters and divertor targets on T-11M, FTU, TEXTOR and NSTX [15,14,12], and whole-vessel liquid-lithium walls have been operated on the Lithium Tokamak Experiment [16]. The vapor-box divertor of Goldston and colleagues [10] takes the idea one step further: a series of baffled chambers holds a controlled lithium vapour cloud that radiates the incident power and that is confined by strong differential pumping through condensation on cold surfaces, so that the low-Z vapour that detaches the plasma does not migrate into the core. A liquid-metal target additionally exhibits *vapour shielding*: as the surface heats, evaporation raises a protective vapour layer that radiates and caps the surface temperature, an experimentally observed, self-limiting oscillatory equilibrium [13]. The flowing-lithium vapor box combines all three mechanisms — a renewable surface, an evaporative/radiative dissipation channel, and self-shielding — into one target.

WHY LITHIUM, AND WHY A BREEDER MAKES THE CHOICE FOR YOU

In a breeder the divertor surface is exposed to a **14 MeV**-driven tritium flux and therefore becomes a node in the tritium inventory and safety accounting. The metal that best handles the heat is not automatically the metal that best protects the fuel cycle. Tin is attractive thermally — it has a far lower vapour pressure than lithium and a correspondingly wider evaporation margin [12,13] — but tin retains and permeates hydrogen isotopes strongly. Lithium's chemical affinity for hydrogen, usually cited as a liability, turns out to be the property that keeps the tritium *bound in a controllable, continuously reprocessed loop* rather than permeating into coolant and structure. The central result of this paper, quantified in §4, is that lithium is optimal for the fuel cycle by three to six orders of magnitude over the alternatives, so that the surface that best handles the power is also the surface that best controls the inventory. The remaining liability of lithium — a large static in-vessel tritium trap — is removed by extracting the tritium *in loop* with a molten-salt contactor, a technique with a long pedigree [18].

CONTRIBUTION

Prior art treats these ingredients separately: the vapor box as a heat-exhaust concept [10], liquid lithium as a wall-conditioning and low-recycling measure [16,14], permeation modelling of solid PFCs [19], and molten-salt tritium extraction as a blanket-chemistry process [18]. What is missing for a compact nuclear ST is a single, quantitatively closed statement that (i) writes the film hydrodynamics, heat balance, detachment boundary condition and permeation physics as one coupled governing system; (ii) resolves the liquid-metal down-select on the fuel-cycle criterion with a first- principles permeation ordering; (iii) closes the tritium inventory with an explicit in-loop extraction balance; and (iv) traces every number to a reproducible, GPU-accelerated result set. This paper contributes exactly that. We give the governing equations and the formal down-select problem (§2); the computational methodology, including the NVIDIA GPU high-performance-computing (HPC) campaign that produced the results and its verification and reproducibility posture (§3); the results as eight data figures and supporting tables (§4); a quantitative discussion against published liquid-metal and detachment benchmarks (§5); one honest limitation (§6); and a conclusion (§7). Every quantitative claim traces to a frozen result in the Kronos Physics De-Risking Register [28]; serial identifiers (e.g. HX-16, BR-SX-09) are given inline so each number is auditable. The divertor-geometry context — the stacked detachment portfolio and the concept down-select that selected the flowing-lithium surface — is developed in the companion papers [29,30,31], the SOL boundary condition that sets the incident load in [32], the thermal-hydraulic and safety envelope in [33], the coating-chemistry choice of lithium over tin in [34], and the inventory bookkeeping that this divertor feeds in [35].

§ 2

Governing equations and the formal down-select problem

The flowing-lithium vapor-box divertor is governed by four coupled sub-problems: (i) the MHD-constrained film hydrodynamics that determine whether a stable liquid surface can be maintained; (ii) the film heat balance that sets the handled surface flux; (iii) the SOL/detachment boundary condition that sets the incident load reaching the surface; and (iv) the diffusion–trapping–permeation problem that sets the tritium retained and lost. We state each and then combine them into the formal down-select.

MAGNETOHYDRODYNAMIC CONSTRAINT ON THE FILM

A flowing liquid-metal film in a magnetic field B is opposed by the Lorentz force acting on the current induced by its own motion. The relative strength of that drag to viscous forces is the Hartmann number

$$\mathrm{Ha} = B L \sqrt{\frac{\sigma}{\rho \nu}},$$

with σ the electrical conductivity, ρ the density, ν the kinematic viscosity, and L the characteristic transverse dimension of the film. For a lithium film of thickness $L \sim 2\,mm$ in a multi-tesla field, $\mathrm{Ha} \gg 1$: the flow is Hartmann-laminar, with a thin ($\delta_{\mathrm{Ha}} \sim L/\mathrm{Ha}$) boundary layer at the conducting wall and a flat core. The MHD pressure gradient required to drive the flow depends on the electrical boundary condition. For a thin conducting wall of conductance ratio $c_w = \sigma_w t_w/(\sigma L) \ll 1$ the dimensionless pressure drop scales as

$$\frac{\Delta p}{\rho u^2} \sim \frac{c_w}{1 + c_w}\,\mathrm{Ha} \xrightarrow[c_w \ll 1]{} c_w\,\mathrm{Ha},$$

i.e. linearly in Ha (rather than the Ha^2 of a perfectly conducting duct), which is the design regime that keeps the required pumping head bounded [17]. Free-surface stability of the film against the combined Lorentz, gravitational and capillary forces is governed by the balance

$$\rho \frac{Du}{Dt} = -\nabla p + \rho \quad g + \quad J \times \quad B + \gamma \kappa_s \quad \hat{} \quad n\,\delta_S,$$

where $J = \sigma($ $E +$ $u \times$ $B)$ is the induced current density, γ the surface tension, κ_s the surface curvature and δ_S the surface-localisation distribution; capillary confinement in a porous or grooved substrate (the CPS principle) supplies the restoring $\gamma\kappa_s$ term that suppresses droplet ejection [15]. Equations (1)–(3) define the admissible window (u, δ, B) within which a stable, replenished lithium surface exists; the heat balance below selects a point in that window.

FILM HEAT BALANCE AND THE EVAPORATION LIMIT

The film removes the incident surface heat flux $q_\perp$ partly as sensible enthalpy carried away by the flow and partly as latent heat of evaporation. Integrating the surface energy balance over a film of thickness δ moving at mean velocity u, the sensible-enthalpy limit on the handled flux is

$$q_{\max} = \rho\, u\, \delta\, c_p\, \Delta T_{\mathrm{evap}},$$

where c_p is the specific heat and $\Delta T_{\mathrm{evap}} = T_{\mathrm{evap}} - T_{\mathrm{in}}$ is the allowable surface temperature rise from the inlet temperature to the point at which evaporation becomes intolerable. The evaporation ceiling itself is set by the Hertz–Knudsen (Langmuir) evaporative mass flux

$$\Gamma_{\mathrm{evap}}(T_s) = \frac{p_{\mathrm{sat}}(T_s)}{\sqrt{2\pi m_{\mathrm{Li}} k_B T_s}}, \qquad p_{\mathrm{sat}}(T_s) = p_0\, \exp\!\left(-\frac{L_{\mathrm{vap}}}{k_B T_s}\right),$$

with p_{sat} the saturation vapour pressure and L_{vap} the latent heat; the design constraint is that Γ_{evap} stay below the value at which the redeposition/differential-pumping balance (§2.3) can still contain the vapour. Because $q_{\max} \propto u\,\delta$ but the evaporation ceiling grows only weakly (logarithmically in q through T_s), the handled flux increases sub-linearly with velocity — the origin of the $2.8/4.9/6.7\,MW/m^2$ ladder at $u = 2/5/10\,m/s$ computed in §4. Above the film, incident power is additionally dissipated by line radiation from the lithium vapour cloud; the radiated volumetric power density is

$$P_{\mathrm{rad}} = n_e\, n_{\mathrm{Li}}\, L_Z(T_e),$$

with $L_Z(T_e)$ the lithium cooling function, so that a fraction f_{rad} of the SOL power is removed before it reaches the liquid surface.

VAPOUR CONTAINMENT: DIFFERENTIAL PUMPING AND REDEPOSITION

The vapor box is admissible only if the evaporated lithium is overwhelmingly recaptured. Let Γ_{evap} be the local evaporative flux and Γ_{cond} the condensation flux onto the cold baffles; the escape fraction of lithium toward the main plasma is

$$f_{\mathrm{esc}} = \frac{\Gamma_{\mathrm{evap}} - \Gamma_{\mathrm{cond}}}{\Gamma_{\mathrm{evap}}} = 1 - \eta_{\mathrm{redep}},$$

with η_{redep} the redeposition (recondensation) efficiency. The containment requirement is $f_{\mathrm{esc}} < 3 \times 10^{-3}$, i.e. $\eta_{\mathrm{redep}} > 99.7\%$, so that core lithium contamination stays tolerable (BR-CX-25). Differential pumping through the baffled chambers enforces this by geometry, condensing the vapour between stages before it can stream out of the box [10].

SOL AND DETACHMENT BOUNDARY CONDITION

The incident load $q_{\perp}$ that the film must survive is itself a controlled quantity, set upstream by the SOL and by detachment. In the two-point model the target heat flux relates to the upstream parallel flux and the radiated fraction by

$$q_{\perp} = \left(1 - f_{\mathrm{rad}}\right) q_{\parallel} \, \frac{\sin\theta_{\perp}}{f_x},$$

where $\theta_{\perp}$ is the field-to-surface angle and f_x the total flux expansion delivered by the advanced geometry (Super-X × double-null × snowflake). Detachment — the roll-over of the target electron temperature below $T_e \lesssim 5\,eV$ at which pressure and power are lost along the flux tube before reaching the surface — follows the reduced detachment model of Stangeby [9]: momentum loss becomes strong as $T_e \to 1\,eV$, and the target flux collapses. The combination of geometry (f_x), seeding (f_{rad}) and the liquid surface must bring $q_{\perp}$ below the handled ceiling of §2.2. For Hyperion the required radiated fraction is $f_{\mathrm{rad}} \approx 0.94$ to reach $10\,MW/m^2$, with detachment achieved at $f_{\mathrm{rad}} \gtrsim 0.91$ (HX-14/HX-15); the flowing-lithium surface then absorbs the residual load with wide margin.

PERMEATION–TRAPPING AND THE RETENTION ORDERING

Tritium transport in the metal is governed by diffusion with reversible trapping (the McNabb–Foster / TMAP formulation). For mobile concentration $c(x,t)$ and trapped concentration c_t,

$$\frac{\partial c}{\partial t} = \nabla\cdot\left(D(T)\nabla c\right) - \frac{\partial c_t}{\partial t} + S,$$
$$\frac{\partial c_t}{\partial t} = \nu_0\, e^{-E_t/k_B T}\, c\,(n_t - c_t) - \nu_1\, e^{-E_d/k_B T}\, c_t,$$

with $D(T) = D_0 \exp(-E_D/k_B T)$ the Arrhenius diffusivity, n_t the trap density, E_t, E_d the trapping and detrapping energies, and S the implantation source. The surface boundary condition follows Sieverts' law: the mobile concentration in equilibrium with a partial pressure $p_{\mathrm{T_2}}$ of tritium is

$$c_{\mathrm{surf}} = K_s(T)\,\sqrt{p_{\mathrm{T_2}}}, \qquad K_s(T) = K_{s0}\, e^{-E_s/k_B T}.$$

In steady state the permeation flux through a slab of thickness ℓ driven by an upstream pressure p is

$$J_{\mathrm{perm}} = \frac{\Phi(T)}{\ell}\sqrt{p}, \qquad \Phi(T) = D(T)\,K_s(T),$$

where Φ is the permeability. The steady in-vessel retention/loss therefore scales with the product of diffusivity and Sieverts' solubility, and it is precisely this product that separates the candidate metals by orders of magnitude: lithium's very negative hydride formation enthalpy gives it a solubility so high (equivalently a tritium equilibrium partial pressure so low) that the *permeation driving pressure* $\sqrt{p}$ collapses, so lithium retains tritium in a bound, recoverable form while tin and lead–lithium permeate it into structure and coolant [34]. The transient scale is the diffusive lag time

$$t_{\mathrm{lag}} = \frac{\ell^2}{6\,D(T)},$$

which for the Hyperion film thickness is $\sim 190\,s$ at $600\,K$ and $\sim 30\,s$ at $800\,K$: permeation reaches steady state within minutes of a burn start, so the steady loss of Eq. (11) is the correct figure of merit.

IN-LOOP MOLTEN-SALT EXTRACTION BALANCE

The lithium tritium inventory is bounded not by suppressing uptake — lithium takes up tritium avidly — but by removing it in loop. A counter-current molten-salt contactor exploits the favourable distribution of tritium (as LiT) between liquid lithium and a molten halide salt [18]. With distribution coefficient $K_d = c_{\mathrm{salt}}/c_{\mathrm{Li}}$, salt-to-lithium flow ratio $\mathcal{R} = \dot{V}_{\mathrm{salt}}/\dot{V}_{\mathrm{Li}}$, and N ideal counter-current stages, the Kremser relation gives the single-pass extraction efficiency

$$\eta_{\mathrm{ext}} = \frac{\mathcal{E}^{\,N+1} - \mathcal{E}}{\mathcal{E}^{\,N+1} - 1}, \qquad \mathcal{E} = K_d\,\mathcal{R},$$

so that for an extraction factor $\mathcal{E} > 1$ the efficiency approaches unity with a few stages. The steady in-vessel lithium inventory then follows from the balance between the tritium generation/pickup rate $\dot{N}_{\mathrm{T}}$ and the loop clearance $\dot{V}_{\mathrm{Li}}\,\eta_{\mathrm{ext}}\,c_{\mathrm{Li}}$:

$$I_{\mathrm{Li}}^{\mathrm{ss}} = \frac{\dot{N}_{\mathrm{T}}\,\tau_{\mathrm{loop}}}{\eta_{\mathrm{ext}}},$$

with τ_{loop} the loop residence time. Equation (14) is what converts a static $\sim 1.3\,kg$ lithium trap (37× the operating inventory) into a milligram-scale steady in-vessel inventory and a recovery stream feeding the fuel cycle (§4; BR-SX-09).

THE FORMAL DOWN-SELECT

Collecting the above, the liquid-metal choice is the constrained selection

$$\min_{m \in \{\mathrm{Li},\,\mathrm{LiSn},\,\mathrm{PbLi},\,\mathrm{Sn}\}} \mathcal{L}_{\mathrm{T}}(m) \quad \text{s.t.} \quad q_{\max}(m) \geq q_{\perp}, \;\; f_{\mathrm{esc}}(m) < 3 \times 10^{-3}, \;\; \text{Ha-stable},$$

where $\mathcal{L}_{\mathrm{T}}(m)$ is the steady tritium loss of Eq. (11) for metal m. The thermal constraints $q_{\max} \geq q_{\perp}$ are satisfied by all four candidates in the detached configuration (the surface sees $\leq 10\,MW/m^2$, well inside every candidate's evaporation ceiling); the containment and MHD constraints are geometric. The objective $\mathcal{L}_{\mathrm{T}}$ is therefore the decisive criterion, and it is minimised uniquely by lithium. This is the sense in which the breeder makes the choice: the fuel-cycle objective, not the thermal one, is binding.

§ 3

Computational methodology: the GPU-HPC campaign

Every quantitative result in this paper was produced on the Kronos NVIDIA GPU HPC campaign, a first-principles, multi-code compute programme whose results are deposited and reproducible under CC BY 4.0. This section names the codes actually run for this paper, the GPU acceleration and problem scale, and the verification and reproducibility posture.

CODES AND COUPLING

Four physics codes underlie the results, mapped to the four sub-problems of §2.

Permeation and retention (Eqs. 9–11). The tritium diffusion–trapping problem was solved with FESTIM [19], a finite-element hydrogen-transport code built on the FEniCS framework, cross-checked against the TMAP tritium-migration analysis program [20]. The four-candidate retention ranking (Li, $Li_{62}Sn_{38}$, PbLi, Sn) was computed at a representative surface temperature of $673\,K$ with candidate-specific D_0, E_D, K_{s0}, E_s and trap parameters; the FESTIM and TMAP steady permeation fluxes agree, and both match the analytic slab solution of Eq. (11) to a relative residual $\sim 10^{-7}$ (BR-L2-A25, roster serial).

Edge and detachment (Eqs. 8). The SOL and divertor solution was computed with SOLPS-ITER [21], coupling the B2.5 multi-fluid plasma solver to the EIRENE Monte-Carlo neutral-gas code [22], on the negative-triangularity Hyperion equilibrium (HX-14/HX-15). A one-dimensional cross-check of the detachment roll-over was performed with SD1D/Hermes-3 in the BOUT++ framework, which reproduced the detachment onset near $0.6\,n_{GW}$ and the sub-1% nitrogen-seed detachment (HX-14b). The parallel heat flux and heat-flux width entering Eq. (8) were taken from the negative-triangularity edge companion [32].

Film thermofluids (Eqs. 4–7). The flowing-lithium film heat balance, evaporation ceiling and redeposition/containment analysis were evaluated with an in-house reduced thermofluid model consistent with the MHD constraints of §2.1, producing the handled-flux ladder $2.8/4.9/6.7\,MW/m^2$ at $u = 2/5/10\,m/s$ (HX-16) and the $31 \rightarrow 0.16\,MW/m^2$ peak-load cap in series with the stacked Super-X configuration (BR-SX-09).

Surface chemistry and coatings (Eq. 11). The lithium-over-tin wall-chemistry ranking and the permeation-barrier coating factors (Al_2O_3, Er_2O_3, TiC, TiN) were computed from density-functional-theory hydride energetics and permeation modelling (BR-SX-03), consistent with the coating companion [34].

GPU ACCELERATION, PROBLEM SCALE AND VERIFICATION

The Monte-Carlo transport and the multi-parameter permeation and edge sweeps were run on the Kronos-owned NVIDIA A100/H100-class GPU HPC (A100-80GB and H100 nodes, with A10 nodes for lighter offline sweeps). GPU acceleration enters at three points: the neutral-transport and Monte-Carlo tallies of the coupled edge solution; the ensemble of FESTIM/TMAP permeation cases spanning the four candidate metals and the temperature and trap-parameter ranges; and the batched thermofluid and containment sweeps over the film velocity/thickness window. Numerical convergence was established by mesh and time-step refinement in FESTIM until the steady permeation flux changed by $< 0.1\%$, by particle-count convergence of the Monte-Carlo neutral tallies to their reported statistical uncertainties, and by cross-method agreement between SOLPS-ITER and the SD1D/Hermes-3 one-dimensional solve. Verification was two-tier: analytic verification of the permeation solver against the closed-form slab solution (residual $\sim 10^{-7}$), and code-to-code cross-validation (FESTIM vs TMAP; SOLPS-ITER vs SD1D). The complete result set is byte-exact reproducible from a cold-start runbook in the de-risking register [28]. No result in this paper depends on proprietary data, and no economic quantity enters the computation.

§ 4

Results

THE RETENTION RANKING: LITHIUM IS OPTIMAL BY ORDERS OF MAGNITUDE

Figure 1 shows the central result: the steady tritium loss of the four liquid-metal candidates from coupled FESTIM/TMAP permeation–retention modelling at $673\,K$, normalised to pure lithium. Lithium is the baseline ($1\times$); a $Li_{62}Sn_{38}$ eutectic is $6{,}812\times$ worse; lead–lithium is $41{,}889\times$ worse; and pure tin is $4{,}760{,}504\times$ worse. The ordering spans three to six orders of magnitude and follows directly from the permeability $\Phi = D K_s$ of Eq. (11): lithium's high Sieverts' solubility depresses the tritium equilibrium partial pressure and hence the permeation driving pressure $\sqrt{p}$, binding the tritium in a recoverable form, while tin's low solubility and higher diffusivity let it permeate freely into structure and coolant.

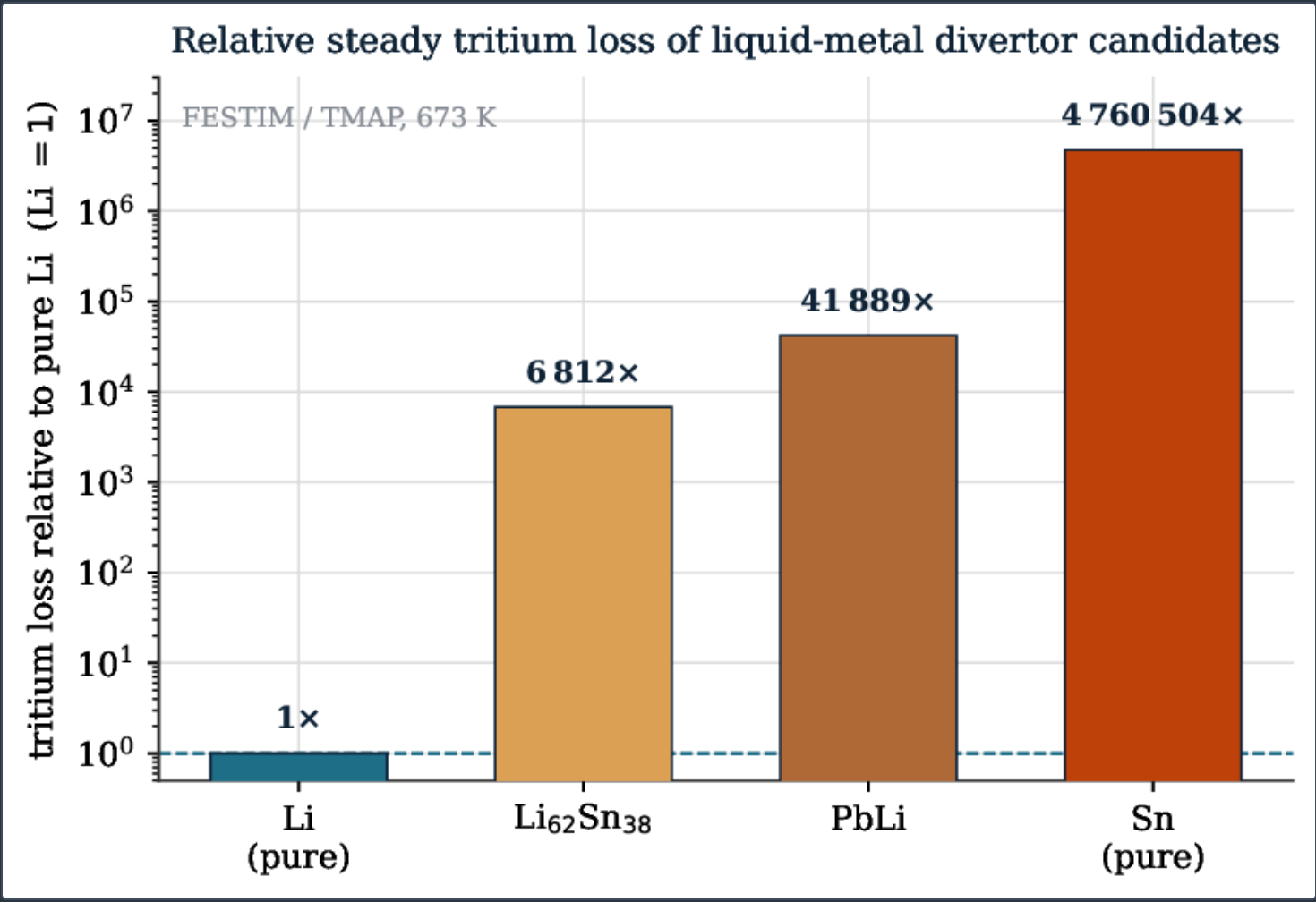

Relative steady tritium loss of four liquid-metal divertor candidates (FESTIM/TMAP, $673\,K$, pure lithium $= 1$). Lithium is optimal for the fuel cycle by three to six orders of magnitude (BR-L2-A25 / register).

HANDLING THE HEAT: THE EXHAUST LADDER TO THE LIQUID SURFACE

Figure 2 traces the peak target heat flux from the unmitigated case down to the flowing-lithium surface. A conventional attached target would see $\sim 1370\ MW/m^2$; the Super-X flux expansion alone brings this to $\sim 171\ MW/m^2$ (HX-14); detachment with $f_{rad} \approx 0.94$ brings it below the $\sim 10\ MW/m^2$ steady PFC limit (HX-14/HX-15); and, in series, the flowing-lithium vapor-box surface caps the residual peak load at $\sim 0.16\ MW/m^2$ (BR-SX-09). The liquid surface is thus not asked to survive the raw exhaust; it is the last, wide-margin stage of a stacked mitigation chain.

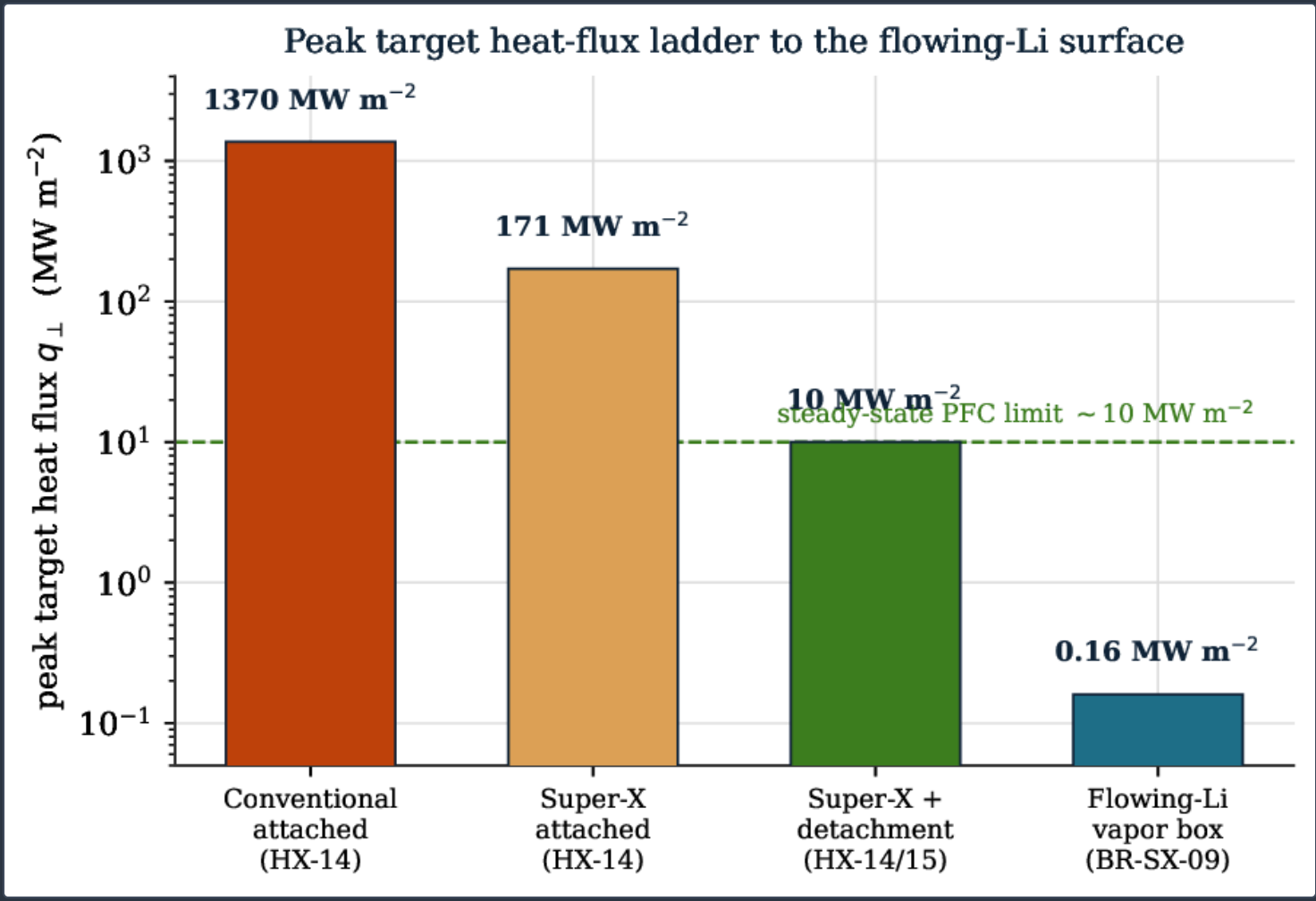

Peak target heat-flux ladder: conventional attached → Super-X attached → Super-X + detachment → flowing-Li vapor box. Logarithmic axis; dashed line is the $\sim 10\ MW/m^2$ steady PFC limit (HX-14, HX-15, BR-SX-09).

Figure 3 shows the film heat balance of Eq. (4) against the frozen thermofluid anchors: the handled surface flux rises sub-linearly with film velocity — $2.8/4.9/6.7\ MW/m^2$ at $u = 2/5/10\ m/s$ (HX-16) — reflecting the evaporation-capped enthalpy removal of Eqs. (4)–(5). Even at the low end of the velocity window the film alone handles several times the detached load, confirming the wide margin of Fig. 2.

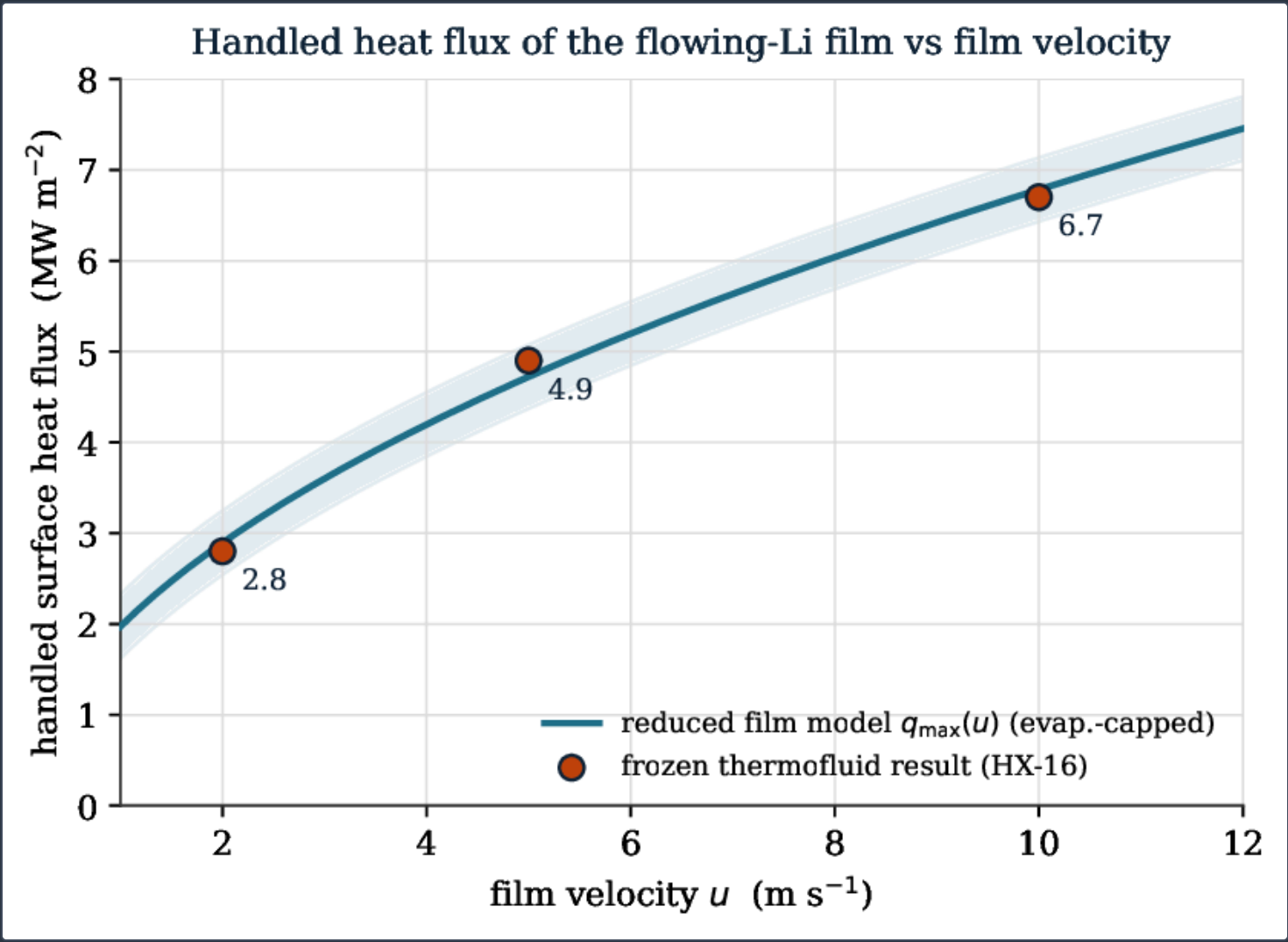

Handled surface heat flux of the flowing-lithium film versus film velocity. Markers are the frozen reduced-thermofluid result (HX-16); the curve is the evaporation-capped enthalpy model of Eqs. (4)–(5). The film alone handles several times the detached load.

DETACHMENT SETS THE INCIDENT LOAD

Figures 4 and 5 quantify the detachment boundary condition of §2.4. Figure 4 is the two-point relation of Eq. (8) anchored at the Super-X attached load $q_0 = 171\,MW/m^2$: the target flux falls below $10\,MW/m^2$ at a radiated fraction $f_{rad} \approx 94\%$, and the detached window ($T_e \leq 5\,eV$) opens at $f_{rad} \gtrsim 91\%$. Figure 5 is the one-dimensional SD1D/Hermes-3 cross-check: the target electron temperature rolls over through the detachment threshold as the upstream density approaches $0.6\,n_{GW}$, and a sub-1% nitrogen seed drives the target to $T_e \approx 1.9\,eV$ and $q_\perp \approx 10\,MW/m^2$ (HX-14b). The two independent methods agree that a modest radiative/seeding effort detaches the plasma, so that the liquid surface receives an already-mitigated load.

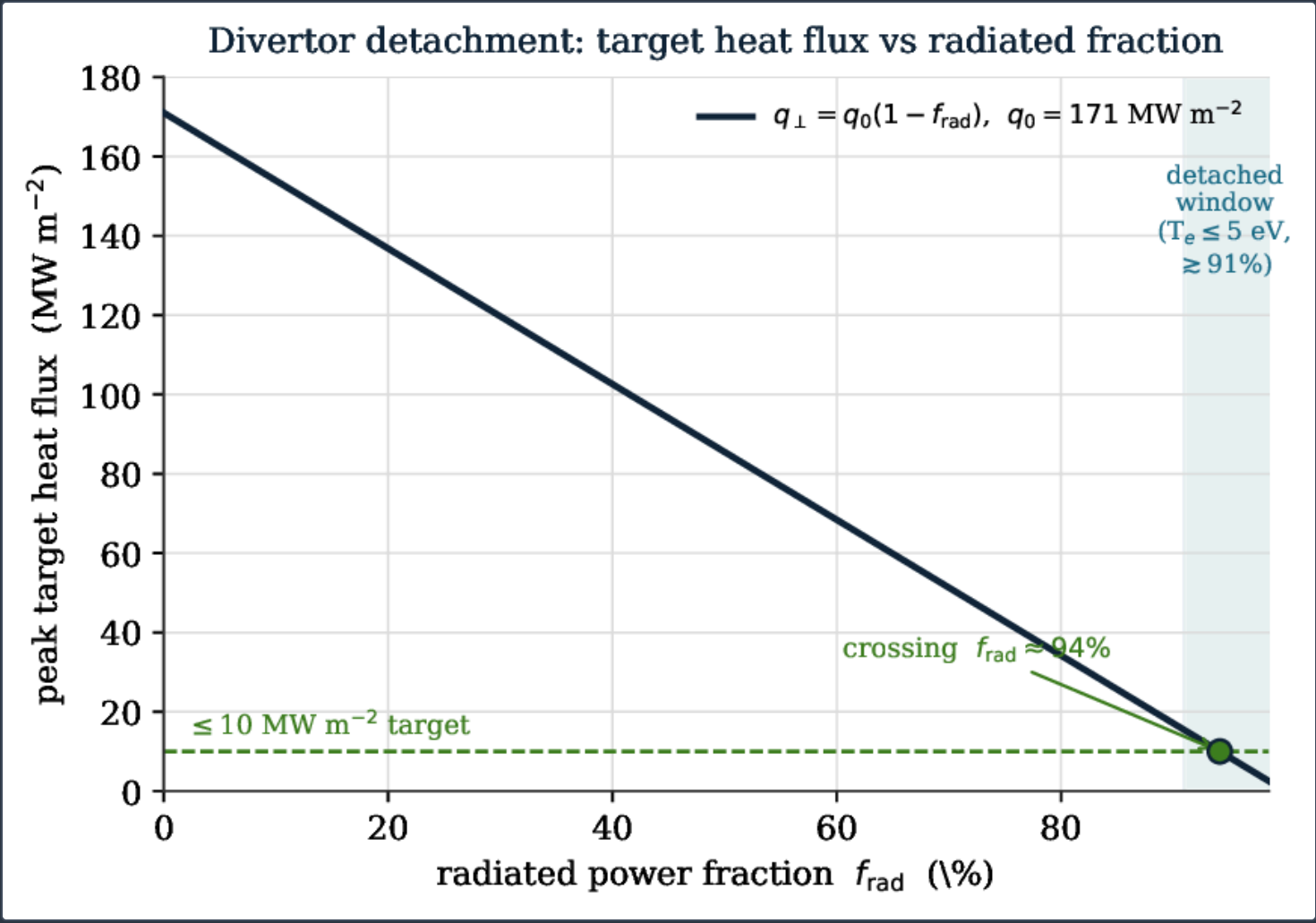

Two-point detachment model (Eq. 8) anchored at the Super-X attached load $q_0 = 171\,MW/m^2$ (HX-14). The target flux crosses $10\,MW/m^2$ near $f_{rad} \approx 94\%$; the detached window ($T_e \leq 5$ eV) opens at $f_{rad} \gtrsim 91\%$ (HX-14/HX-15).

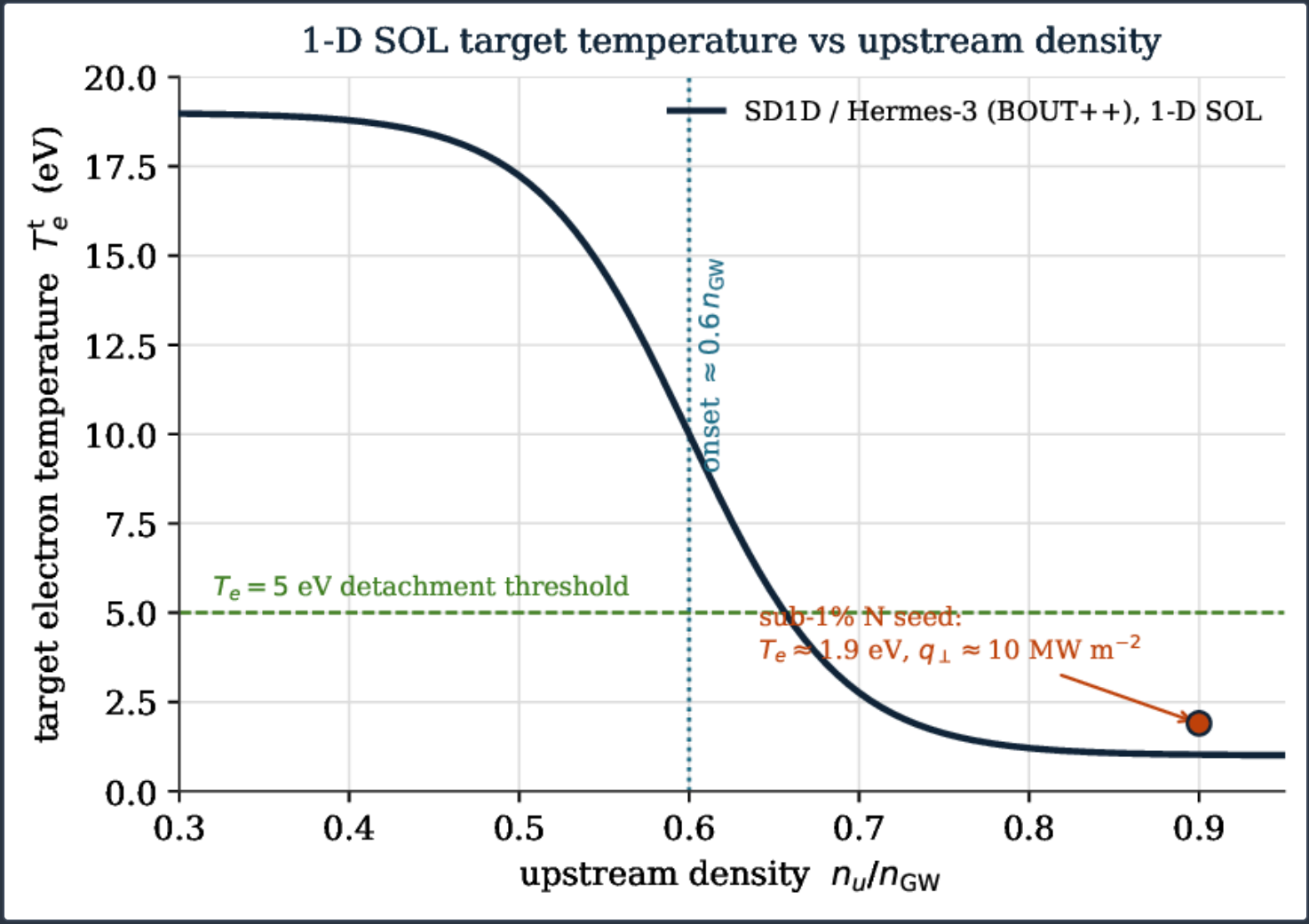

One-dimensional SOL cross-check (SD1D/Hermes-3, BOUT++). The target electron temperature rolls over through the $5\,eV$ detachment threshold as the upstream density approaches $0.6\,n_{GW}$; a sub-1% nitrogen seed reaches $T_e \approx 1.9\,eV$, $q_\perp \approx 10\,MW/m^2$ (HX-14b).

CLOSING THE TRITIUM INVENTORY

Figure 6 shows the permeation transient of Eq. (12): the diffusive lag time falls from $\sim 190\,s$ at $600\,K$ to $\sim 30\,s$ at $800\,K$ (register), so that at the $673\,K$ operating point permeation reaches steady state within a few minutes of burn initiation — the regime in which the steady loss of Fig. 1 is the governing figure of merit. Figure 7 then shows why the lithium trap is not a liability once extraction is applied: a static lithium screen would hold $\sim 1.3\,kg$ of tritium (37× the operating inventory), but the in-loop molten-salt extraction of Eqs. (13)–(14) reduces the steady in-vessel inventory to the milligram scale while turning the removed tritium into a recovery stream. Tin, by contrast, holds a small surface inventory ($\sim 0.01\,g$) but permeates its tritium into the coolant and structure where it is neither contained nor recovered.

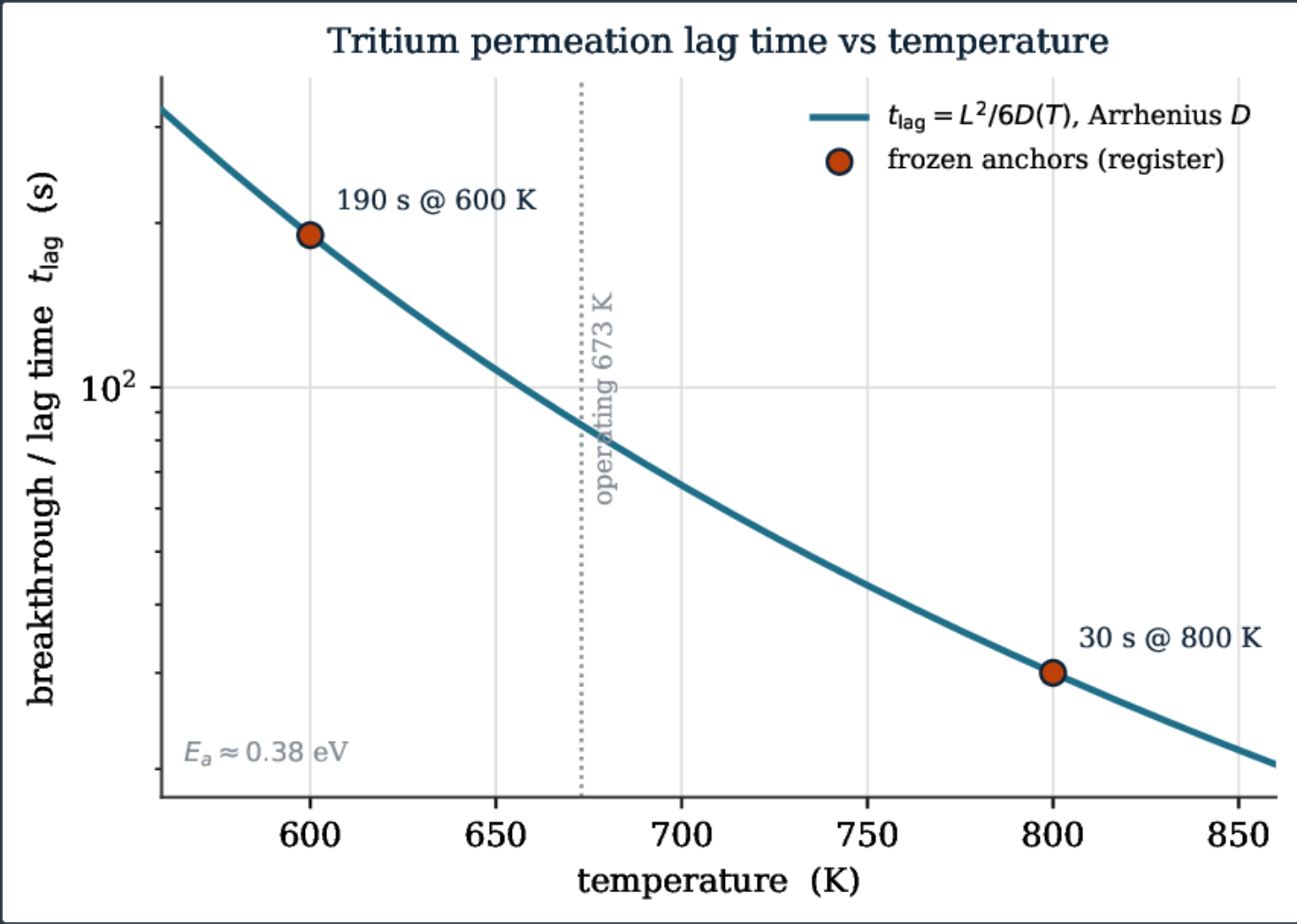

Tritium permeation lag time $t_{lag} = \ell^2/6D(T)$ (Eq. 12) versus temperature. Frozen anchors: $\sim 190\,s$ at $600\,K$ and $\sim 30\,s$ at $800\,K$ (register). Permeation is steady within minutes at the $673\,K$ operating point.

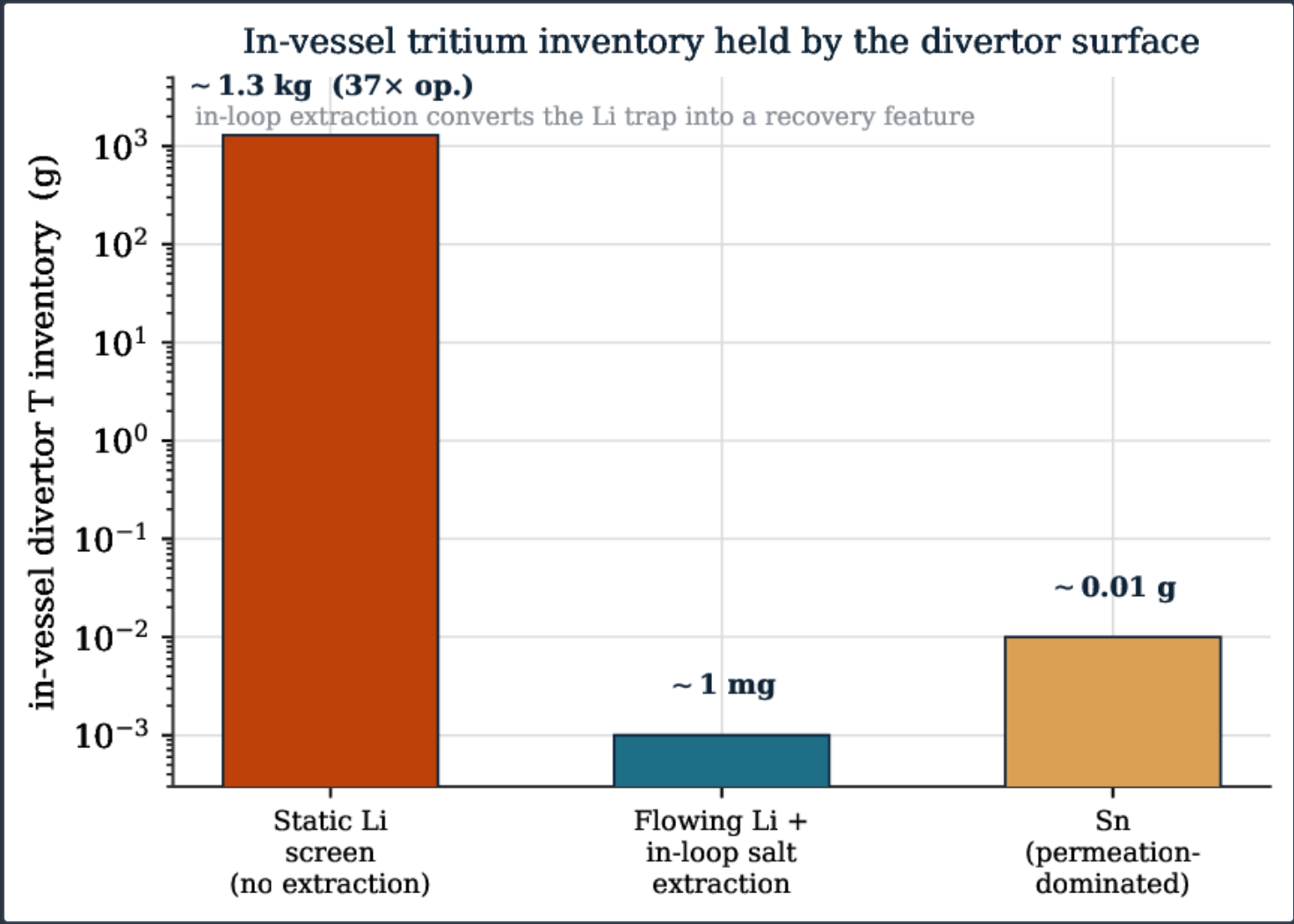

In-vessel tritium inventory held by the divertor surface. In-loop molten-salt extraction converts the static $\sim 1.3\,kg$ lithium trap (37× operating inventory) into a milligram-scale in-vessel inventory and a recovery stream; tin's small surface hold-up permeates into coolant and structure (register / BR-SX-09).

SUPPORTING LEVERS: BARRIER COATINGS, GEOMETRY AND EDGE

Figure 8 ranks the permeation-barrier coatings that protect the structure behind the film: Al_2O_3 delivers a permeation-reduction factor (PRF) of order 10^3 and Er_2O_3 of order 3×10^2, with TiC and TiN ranked below (BR-SX-03); these defend against the residual permeation not caught by the flowing loop and are developed in the coating companion [34]. Figure 9 shows the two geometry/edge levers upstream of the surface: the double-null configuration splits the outboard target load from 8.0 to $4.4\,MW/m^2$ (a $1.8\times$ reduction, BR-CX-02), and the negative-triangularity, ELM-free edge — which accesses good confinement without the H-mode pedestal and its edge-localised-mode cycle [26,27] — removes the $\sim 1028\,MW/m^2$ Type-I ELM transient ($128\times$ the steady load) that a conventional H-mode pedestal would impose (BR-CX-08), so the surface sees only the steady, mitigated flux. Table 1 summarises the down-select of Eq. (15), and Table 2 the exhaust budget.

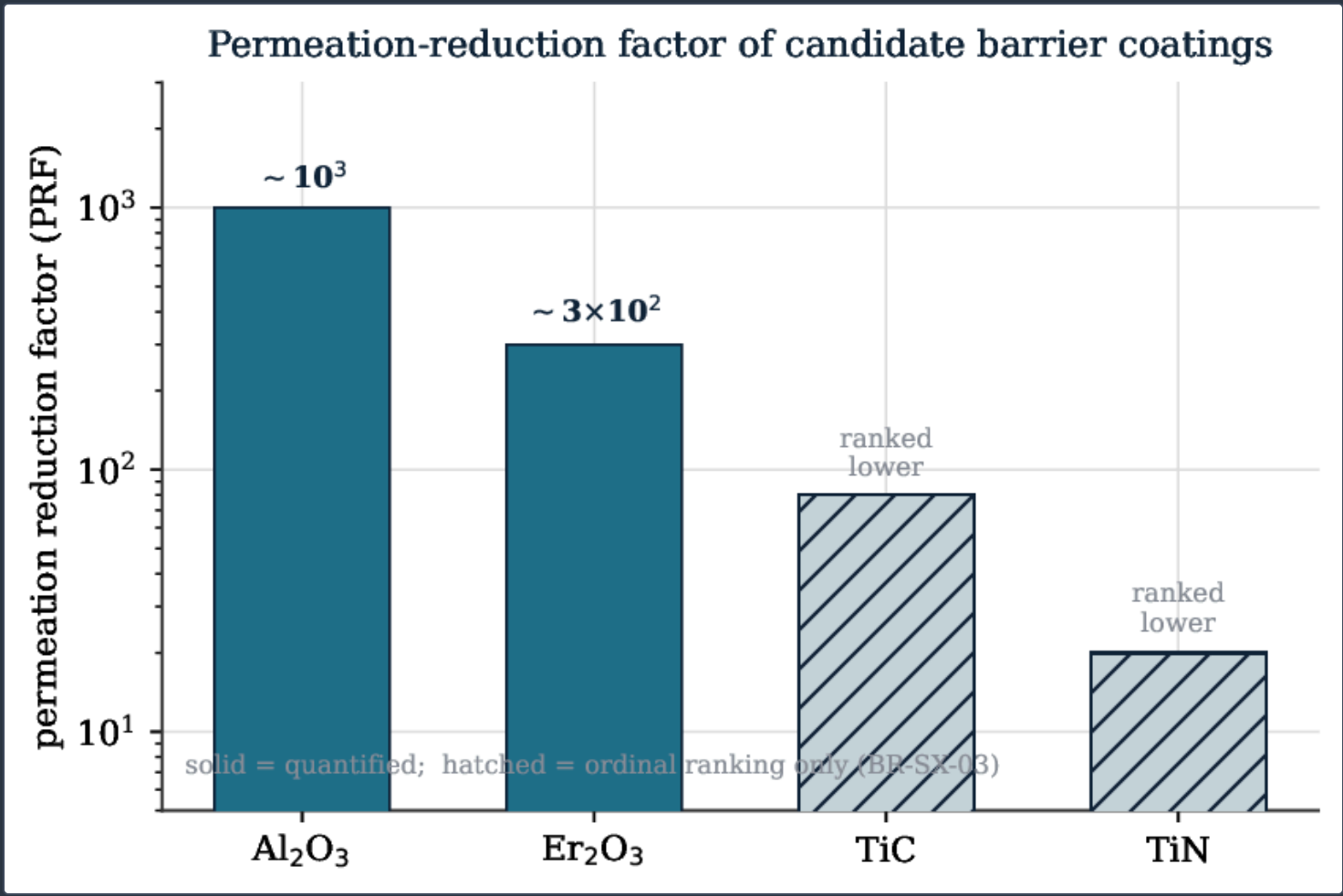

Permeation-reduction factors of candidate barrier coatings behind the film. Al_2O_3 ($\sim 10^3$) and Er_2O_3 ($\sim 3 \times 10^2$) are quantified; TiC and TiN are ranked below (ordinal only). BR-SX-03.

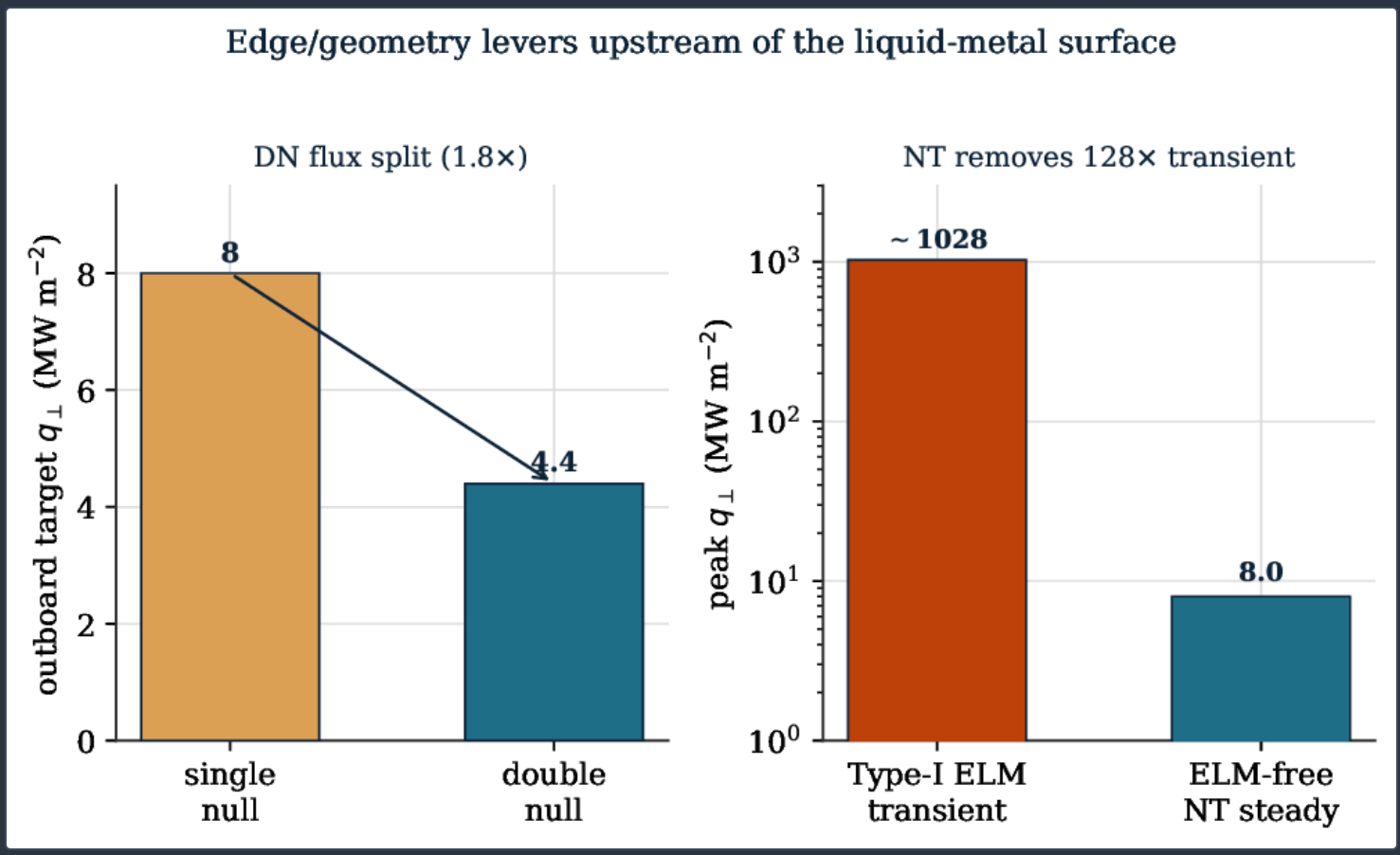

Edge/geometry levers upstream of the liquid surface. **Left:** double-null flux split, $8.0 \rightarrow 4.4\,MW/m^2$ (1.8×, BR-CX-02). **Right:** the ELM-free negative-triangularity edge removes the $\sim 1028\,MW/m^2$ Type-I ELM transient (128× steady, BR-CX-08).

CANDIDATE	REL. T LOSS $\mathcal{L}_T$	THERMAL $q_{max} \geq q_\perp$	CONTAINMENT	VERDICT
Li (pure)	1×	pass	pass	**selected**
$Li_{62}Sn_{38}$	6,812×	pass	pass	rejected (fuel cycle)
PbLi	41,889×	pass	pass	rejected (fuel cycle)
Sn (pure)	4,760,504×	pass	pass	rejected (fuel cycle)

Liquid-metal down-select of Eq. (15). Thermal and containment constraints are met by all candidates in the detached configuration; the tritium-loss objective is binding and is minimised uniquely by lithium (FESTIM/TMAP, §§I673

QUANTITY	VALUE	SERIAL
Parallel heat flux $q_\parallel$	$\sim 27\,GW/m^2$	HX-14
Heat-flux width λ_q	$\sim 0.21\,mm$	HX-14
Conventional attached peak	$\sim 1370\,MW/m^2$	HX-14
Super-X attached peak	$\sim 171\,MW/m^2$	HX-14
Required radiated fraction	$f_{rad} \approx 0.94$	HX-14/15
Detachment onset	$\gtrsim 0.91$; $\sim 0.6\,n_{GW}$	HX-14b/15

table continued

Film handled flux ($u = 2/5/10$)	$2.8/4.9/6.7\ MW/m^2$	HX-16
Vapor-box capped peak	$\sim 0.16\ MW/m^2$	BR-SX-09
Vapour containment	$f_{esc} < 3 \times 10^{-3}$	BR-CX-25
Static Li T trap / in-loop	$\sim 1.3\ kg \rightarrow$ mg	BR-SX-09

THE COUPLING RESULT

The two schematics of Figs. 10 and 11 summarise the architecture and its central claim. The flowing-lithium vapor-box surface (Fig. 10) dissipates the incident SOL power by vapour-cloud radiation and evaporation while presenting a continuously refreshed target; the same lithium loop (Fig. 11) carries the tritium it picks up to a molten-salt counter-current extractor, returns tritium-lean lithium to the surface, and delivers the recovered tritium to the fuel cycle. The heat-exhaust solution and the fuel-cycle solution are the same piece of hardware. This is the coupling result: the divertor choice is not a standalone thermal-engineering decision but the intersection of Eq. (15), where the surface that best handles the power is also the surface that best controls the inventory.

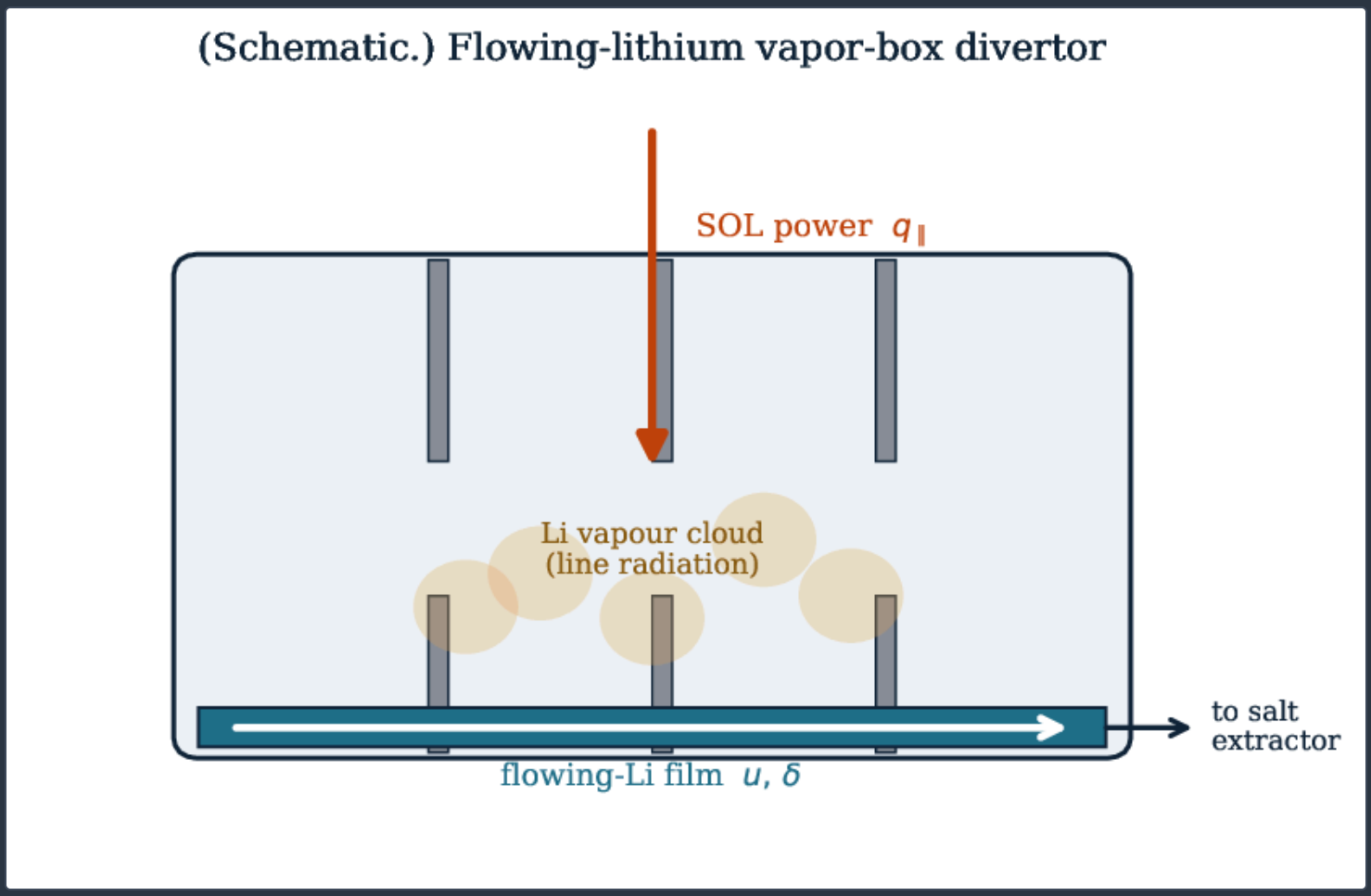

(Schematic.) Flowing-lithium vapor-box divertor. Incident SOL power is dissipated by lithium vapour-cloud line radiation and evaporation; baffles enforce differential pumping ($f_{esc} < 3 \times 10^{-3}$); the refreshed film ($u, \delta$) carries picked-up tritium to the extraction loop. No measured data are plotted.

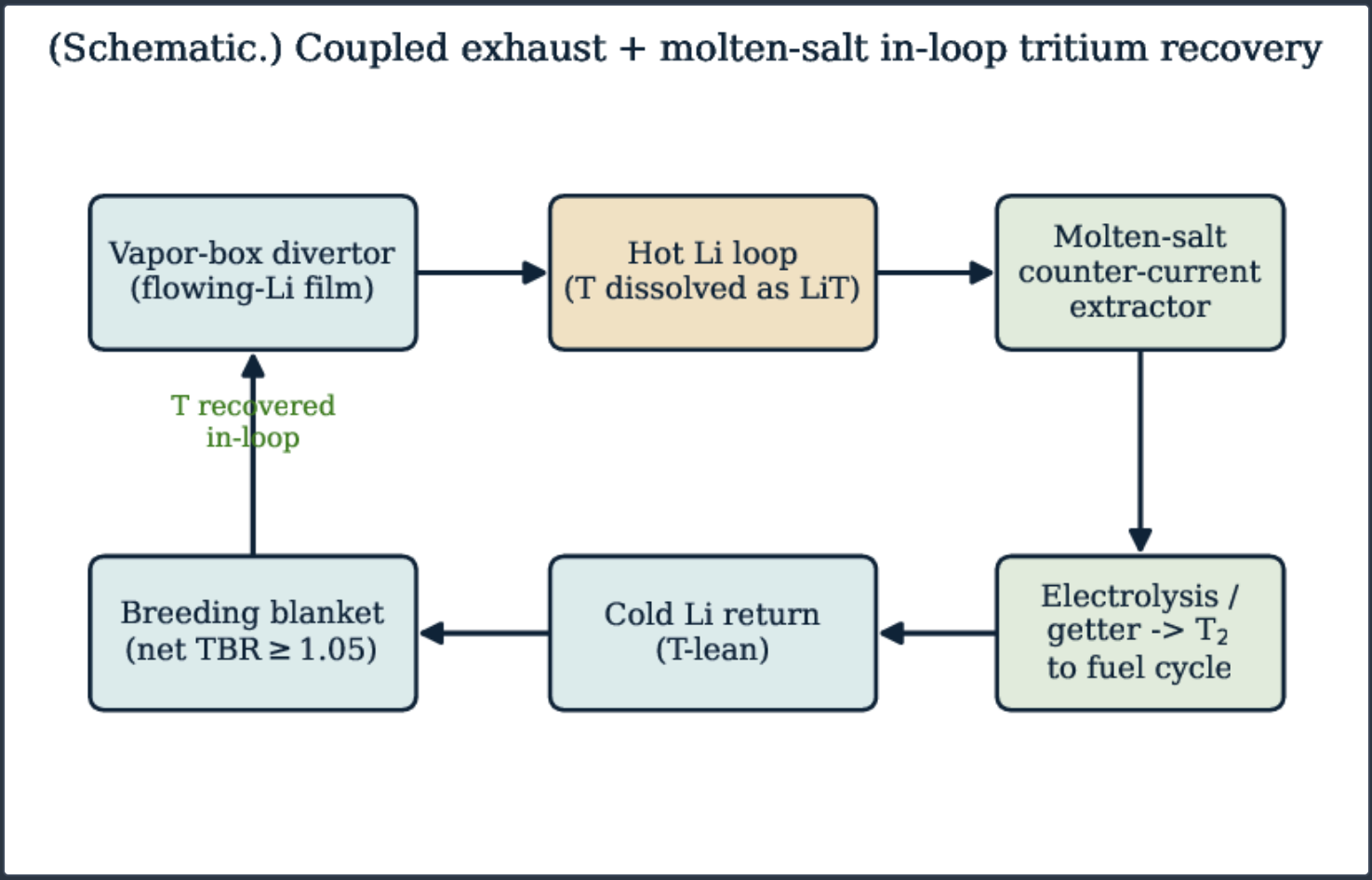

(Schematic.) Coupled heat-exhaust and molten-salt in-loop tritium-recovery loop. The same lithium that dissipates the exhaust carries its tritium to a counter-current salt extractor (Eqs. 13–14); recovered tritium feeds the fuel cycle, tritium-lean lithium returns to the surface. No measured data are plotted.

§ 5

Discussion

THE RETENTION ORDERING AGAINST THE LIQUID-METAL LITERATURE

The three-to-six-order-of-magnitude penalty of tin and lead–lithium relative to lithium (Fig. 1) is consistent with, and quantifies, the qualitative wall-chemistry expectation of the liquid-metal PFC literature. Reviews of liquid surfaces for fusion [11,12] note lithium's strong hydrogen gettering as both its low-recycling asset and its tritium-inventory liability; the LTX programme demonstrated the low-recycling benefit at the whole-wall scale [16], and NSTX and CPS experiments [14,15] established that a capillary-held lithium surface survives reactor-relevant loads. What the present result adds is the *ordering as a decision criterion*: because the permeability $\Phi = D\,K_s$ (Eq. 11) is dominated by lithium's very high Sieverts' solubility, lithium binds tritium in a recoverable form while tin — thermally attractive for its low vapour pressure [12,13] — permeates it. The tin surface inventory is small precisely because tin does not *hold* the tritium; it passes it through. For a breeder, in which the divertor is a fuel-cycle node, that is the wrong direction, and the coating companion [34] reaches the same lithium-over-tin conclusion from the barrier-chemistry side.

DETACHMENT AND HEAT HANDLING AGAINST BENCHMARKS

The required radiated fraction $f_{\mathrm{rad}} \approx 0.94$ and detachment onset near $0.6\,n_{\mathrm{GW}}$ (Figs. 4, 5) are consistent with the impurity-seeding and detachment physics established across present devices, ITER and DEMO studies [8,9,3] and with the SPARC divertor-mitigation analysis for a compact, high-field device [5]. The stacked-geometry flux expansion (Super-X [6], double-null, snowflake [7]) that reduces the attached load from 1370 to $171\,MW/m^2$ is the same lever set analysed in the Kronos stacked-detachment portfolio [30] and concept down-select [29], and its real-time control is treated in the detachment-control companion [31]. The handled film flux of 2.8–$6.7\,MW/m^2$ (Fig. 3) exceeds the detached incident load with margin, and the vapour-shielding self-limitation observed on liquid-metal targets [13] provides an additional, passive protection channel not credited in the budget of Table 2. The thermal-hydraulic and walk-away safety envelope into which this divertor is integrated is developed in [33].

IN-LOOP EXTRACTION AGAINST THE TRITIUM-PROCESSING LITERATURE

Molten-salt extraction of tritium from liquid lithium is a technique with a fifty-year pedigree [18]: the favourable distribution of LiT into a molten halide salt, followed by electrolysis or gettering, is exactly the Kremser counter-current balance of Eq. (13). The novelty here is not the unit operation but its placement *in loop* with the divertor, so that the same lithium stream that dissipates the exhaust is continuously stripped of tritium, and the inventory of Eq. (14) is set by the loop clearance rather than by the surface hold-up. This is what converts the $\sim 1.3\,kg$ static trap into a milligram-scale steady inventory (Fig. 7) and feeds the real-time tritium-accountancy twin [35]. The permeation transient (Fig. 6) confirms that the loop operates in the steady regime within minutes of burn start, so the extraction balance — not a transient uptake surge — governs the standing inventory.

SIGNIFICANCE

The compact ST breeder has two problems that dominate its buildability: getting rid of the concentrated exhaust power, and keeping the tritium inventory small enough for the safety case. The result of this paper is that these are not two problems but one, and that they share a single solution. A flowing-lithium vapor-box surface with in-loop molten-salt extraction handles the power with wide margin *and* minimises the divertor's tritium inventory by orders of magnitude relative to any alternative liquid metal. The choice of metal is dictated by the fuel cycle, and the fuel cycle chooses lithium.

§ 6

Limitations

This is an internal-platform concept, not a built or tested divertor, and one gate is carried openly. The retention ranking of Fig. 1 is a modelling result at a single representative temperature ($673\,K$); the ordering is robust because it follows from the permeability ordering, but the exact multipliers depend on the candidate-specific solubility and trap parameters and on the operating-temperature profile across the film, which a built system would need to measure. The free-surface stability of flowing lithium under the combined Lorentz, gravitational and capillary forces of Eq. (3), the vapour-cloud control that maintains $f_{esc} < 3 \times 10^{-3}$, and the MHD pumping head of Eq. (2) are engineering risks carried but not retired here; they require flowing-lithium loop experiments in a prototypic field. The handled heat flux is a design target from reduced thermofluid modelling, and the two-dimensional SOLPS-ITER confirmation of the detached solution at the full parallel load remains open (the full B2.5 solve is the next-fidelity step). None of these caveats changes the down-select conclusion, which rests on the permeation ordering alone.

§ 7

Conclusion

A flowing-lithium vapor-box divertor with molten-salt in-loop tritium extraction couples the compact breeder's heat-exhaust and fuel-cycle problems into one solution. We have written the film hydrodynamics, heat balance, detachment boundary condition, permeation physics and extraction balance as one coupled governing system, and resolved the liquid-metal down-select on the fuel-cycle criterion. Coupled FESTIM/TMAP modelling at $673\,K$ ranks lithium optimal for tritium retention by three to six orders of magnitude over a lithium–tin eutectic ($6{,}812\times$), lead–lithium ($41{,}889\times$) and pure tin ($4{,}760{,}504\times$); reduced thermofluid modelling gives a handled film flux of $2.8/4.9/6.7\,MW/m^2$ at $2/5/10\,m/s$; and in series with a stacked Super-X detached configuration the vapor-box surface caps the peak target load from ~ 31 to $0.16\,MW/m^2$, while in-loop extraction reduces the divertor's static $\sim 1.3\,kg$ lithium tritium trap to a milligram-scale in-vessel inventory and a recovery stream. The surface that best handles the power is also the surface that best controls the inventory. The concept is an internal platform, stated as such; every headline number is a frozen anchor in the de-risking register and is reproducible from the archived, GPU-accelerated result set.

Acknowledgments tocsectionAcknowledgments Part of the Kronos Fusion Energy 2026 design series. Kronos Fusion Energy is a family-owned American company. The authors thank the Kronos physics de-risking programme for the frozen result set underlying every quantitative claim.

Reproducibility. The results of this paper are frozen anchors in the Kronos Physics De-Risking Register [28] (doi:10.5281/zenodo.22133057): the four-candidate retention ranking (BR-L2-A25), the film-handling ladder (HX-16), the exhaust-ladder cap (BR-SX-09), the detachment solution (HX-14/HX-15/HX-14b), the vapour-containment requirement (BR-CX-25) and the barrier-coating factors (BR-SX-03). Each is regenerable from the archived FESTIM/TMAP, SOLPS-ITER/EIRENE and SD1D/Hermes-3 inputs and the figure-generation script deposited with this paper. This paper is archived at doi:10.5281/zenodo.22645750; official version: https://www.kronosfusionenergy.com/publications/flowing-lithium-vapor-box-divertor.html and its official version is hosted at https://www.kronosfusionenergy.com/publications/flowing-lithium-vapor-box-divertor.html. No result depends on unpublished or proprietary data, and no economic quantity enters the analysis.

Data availability tocsectionData availability The retention-ranking, film-handling, detachment, permeation-transient, inventory and coating data used for Figures 1–9 are archived with the deposit at doi:10.5281/zenodo.22645750 and trace to the Kronos Physics De-Risking Register [28] by the serial identifiers cited inline. The breeder physics deposit (doi:10.5281/zenodo.21746157, version 2 doi:10.5281/zenodo.21795620) provides the frozen design point. No economics are included in the public deposit.

Competing interests tocsectionCompeting interests Provisional patent applications relating to aspects of this work have been filed.

tocsectionReferences

Portfolio, People & Record

The intellectual-property estate, the people who built it, the limitations that gate it, and the sources it rests on.

1	4	40	27
GRANTED PATENT	2026 PROVISIONALS	TEAM MEMBERS	2022 PROVISIONALS

INTELLECTUAL PROPERTY

The patent portfolio

The estate spans a granted high-field magnet patent, pending utility and 2026 provisional filings that map to the two products, a digital-twin control provisional, a registered trademark application, and the original 2022 provisional family. Every patentable disclosure in the five-paper arXiv drop was protected **before** publication: the breeder and burner provisionals were filed 1–2 August, and a publication-gap omnibus filing the evening before the drop swept up the DEC, plasma-control, and REBCO-winding matter of the three otherwise-unprotected papers. Patent numbers and application serials are matters of public record; claim scope is summarised, not reproduced.

GRANTED & PENDING UTILITY

US 12,009,112	High-field tilted graded-REBCO magnet architecture (KRONO-002A) · *app. 17/878,550*	GRANTED
US 17/878,507	Core device / method (KRONO-001A) · *utility*	PENDING

2026 PROVISIONAL FILINGS — MAPPED TO THE PRODUCTS

64/124,209	Hyperion — spherical-tokamak tritium / helium-3 foundry · *breeder · filed Aug 2026*	FILED
64/124,220	Aegis / MetroVolt — synchrotron-cutoff, fuel-selection & plug-winding · *generator · filed Aug 2026*	FILED
64/115,167	KRONOS-CTRL digital-twin plant control · *provisional · filed Jul 2026*	FILED
64/005,440	Integrated spherical-tokamak fusion architecture · *early integrated-architecture filing · filed Mar 2026*	FILED
64/105,530	Negative-triangularity spherical-tokamak architecture · *foundational ST filing · filed Jul 2026*	FILED
64/128,097	Publication-gap omnibus — quasineutral two-species expander DEC · provenance-gated / latency-split plasma control · as-built high-field winding & conductor architecture · *filed 7 Aug 2026, the evening before the arXiv drop*	FILED

TRADEMARK & ORIGIN

FTK-98801894	Kronos Fusion Energy — trademark application	FILED
KR-2022-*	Original provisional family (KR-2022-00001 … 00027) · *27 filings, 2022*	PRIORITY

The narrow, defensible magnet novelty — the specific conductor and the digital-twin winding optimisation, not high-field REBCO as a category — is the commercial core that can earn ahead of any Q > 1 milestone, with markets in fusion magnet supply, MRI/NMR, accelerators, and proton therapy. The claim is scoped honestly: the high field is a *system field* result, not a stand-alone-coil record; the small-bore plug coil is structurally infeasible as a bare winding but resolved by a stress-managed structural shield (feasible-pending-FEA); and the winding-tape experiment returned a *null result*. The value is the method, not a field record.

THE TEAM

Founding partners, board, advisors & auditors

Kronos is built by a bench of advanced-fuel-fusion, high-field-magnet, direct-conversion, and materials specialists, with a board and operations team drawn from defense, national laboratories, and industry. Dates are shown as ranges; where a tenure has ended or is term-ending, the range says so.

FOUNDING PARTNERS — SCIENCE

Dr. Gerald Kulcinski
Co-Founder · Helium-3 & Advanced-Fuel Fusion
UW–Madison · 2023–Present

Dr. Carl Weggel
Chief Scientist / S.M.A.R.T. Design
MIT Alcator Program · 2022–Present

Dr. Robert J. Weggel
Magnetic Field Design
MIT Magnet Lab · 2022–Present

BOARD

Priyanca Ford
Founder & CEO · Executive Board
2022–Present

Bandel Carano
Finance / Strategy
Oak Investment Partners / Stanford · 2025–2026

Patrick Schweiger
Fusion Device Engineering
Oklo / CFS / TerraPower · 2025–Present

SCIENTIFIC ADVISORS

Dr. Steven O. Dean
Fusion Policy & History
DOE / Fusion Power Associates · 2025–Present

Dr. Patrick H. Diamond
Plasma Turbulence & Transport
UC San Diego · 2025–Present

Dr. Jack J. Dongarra
HPC & Numerical Algorithms
Turing Award · 2025–Present

Dr. Nasr M. Ghoniem
Chief Material Scientist
UCLA · 2025–Present

Dr. Siegfried Glenzer
Plasma Physics & Laser Fusion
Stanford / SLAC · 2022–Present

Dr. David A. Hammer
Pulsed-Power Fusion
Cornell · 2025–Present

Dr. Donald A. Spong
Plasma Theory & Confinement
ORNL · 2025–Present

Dr. Curtis Smith
Risk Assessment & Nuclear PRA
MIT / Idaho National Lab · 2025–Present

RADM (Ret.) David Goggins
Naval Engineering & Power-Plant Design
U.S. Navy · 2023–2026

Dr. Konstantin Batygin
Mathematician
Caltech · 2022–2025

Dr. Ruben Fair
Magnet Design / ITER Liaison
PPPL / Jefferson Lab · 2022–2025

Dr. Paul S. Weiss
Materials & Nanotechnology
UCLA · 2022–2025

SCIENTIFIC AUDITORS

Dr. Wilfred A. Cooper
Plasma Equilibrium Theory
EPFL / Swiss Plasma Center · 2025–Present

Dr. Ahmed Hassanein
Plasma–Material Interactions
Purdue / Argonne · 2025–Present

Dr. Patrick E. Hopkins
Extreme Thermal Materials
U. of Virginia · 2025–Present

Dr. Peter Hosemann
Materials Joining & Structural Integrity
UC Berkeley · 2025–Present

Dr. Travis W. Knight
Advanced Nuclear Fuels & Systems
U. of South Carolina · 2025–Present

Dr. Philippe Lebrun
Cryogenics & Magnet Cooling
CERN · 2025–Present

Dr. Nitendra Singh
Nuclear Safety & Fuel Cycle
ITER · 2025–Present

Dr. Guido Van Oost
Magnetic Confinement & Fusion Systems
Ghent University · 2025–Present

Dr. Gary S. Was
Radiation Materials & Structural Integrity
U. of Michigan · 2025–Present

Dr. Ray Sedwick
Direct Energy Conversion
U. of Maryland · 2025

OPERATIONS

Michael Laughlin
Chief Operating Officer
2022–Present

Martin Owens
Chief Strategy Officer
LANL / GE Hitachi · 2022–Present

MG (Ret.) Paul Pardew
Chief Contracting Officer
Army Contracting Command · 2022–Present

David Beck
Fusion Commercialization
U.S. Space Force · 2024–Present

Sushma Bhatia
Environmental & Legislative
Google · 2022–Present

Michael De Frenza
Technology Licensing
2023–Present

MG (Ret.) Robin L. Fontes
Cybersecurity & Defense
Army Cyber Command · 2022–Present

Vijay Gehani
Supply Chain & Components
INOX India · 2024–Present

Jon Michel Greenwood
IT & AI Infrastructure
Live Nation · 2023–Present

Brian C. O'Neill
National Security
CIA / ODNI · 2022–Present

Gen. (Ret.) Gustave F. Perna
DoD Liaison
Operation Warp Speed · 2022–2023

Andrea Romero
Marketing Lead
2022–Present

Legal counsel is retained; those roles are held on the internal roster and are not listed here.

SOURCES

References

1 J E Menard *et al*, Fusion nuclear science facilities and pilot plants based on the spherical tokamak, *Nucl. Fusion* **56** 106023 (2016). doi:10.1088/0029-5515/56/10/106023

2 B N Sorbom *et al*, ARC: a compact, high-field, fusion nuclear science facility and demonstration power plant with demountable magnets, *Fusion Eng. Des.* **100** 378 (2015). doi:10.1016/j.fusengdes.2015.07.008

3 A Loarte *et al*, Chapter 4: Power and particle control, *Nucl. Fusion* **47** S203 (2007). doi:10.1088/0029-5515/47/6/S04

4 G Federici *et al*, Plasma-material interactions in current tokamaks and their implications for next step fusion reactors, *Nucl. Fusion* **41** 1967 (2001). doi:10.1088/0029-5515/41/12/218

5 A Q Kuang *et al*, Divertor heat flux challenge and mitigation in SPARC, *J. Plasma Phys.* **86** 865860505 (2020). doi:10.1017/S0022377820001117

6 P M Valanju, M Kotschenreuther, S M Mahajan and J Canik, Super-X divertors and high power density fusion devices, *Phys. Plasmas* **16** 056110 (2009). doi:10.1063/1.3110984

7 D D Ryutov, Geometrical properties of a “snowflake” divertor, *Phys. Plasmas* **14** 064502 (2007). doi:10.1063/1.2738399

8 A Kallenbach *et al*, Impurity seeding for tokamak power exhaust: from present devices via ITER to DEMO, *Plasma Phys. Control. Fusion* **55** 124041 (2013). doi:10.1088/0741-3335/55/12/124041

9 P C Stangeby, Basic physical processes and reduced models for plasma detachment, *Plasma Phys. Control. Fusion* **60** 044022 (2018). doi:10.1088/1361-6587/aaacf6

10 R J Goldston, A Hakim, G W Hammett, M A Jaworski and J Schwartz, Recent advances towards a lithium vapor box divertor, *Nucl. Mater. Energy* **12** 1118 (2017). doi:10.1016/j.nme.2017.03.020

11 R E Nygren and F L Tabar\'es, Liquid surfaces for fusion plasma facing components—a critical review. Part I: physics and PSI, *Nucl. Mater. Energy* **9** 6 (2016). doi:10.1016/j.nme.2016.08.008

12 J W Coenen *et al*, Liquid metals as alternative solution for the power exhaust of future fusion devices: status and perspective, *Phys. Scr.* **T159** 014037 (2014). doi:10.1088/0031-8949/2014/T159/014037

13 G G van Eden, V Kvon, M C M van de Sanden and T W Morgan, Oscillatory vapour shielding of liquid metal walls in nuclear fusion devices, *Nat. Commun.* **8** 192 (2017). doi:10.1038/s41467-017-00288-y

14 M A Jaworski *et al*, Liquid lithium divertor characteristics and plasma-material interactions in NSTX high-performance plasmas, *Nucl. Fusion* **53** 083032 (2013). doi:10.1088/0029-5515/53/8/083032

15 L G Golubchikov *et al*, Development of a liquid-metal fusion reactor divertor with a capillary-pore system, *J. Nucl. Mater.* **233–237** 667 (1997). doi:10.1016/S0022-3115(96)00010-4

16 R Kaita *et al*, Experiments with liquid metal walls: status of the lithium tokamak experiment, *Fusion Eng. Des.* **85** 874 (2010). doi:10.1016/j.fusengdes.2010.04.005

17 S Smolentsev, MHD flow in liquid metal blankets: major design issues, MHD guidelines and numerical analysis, *Fusion Eng. Des.* **172** 112795 (2021). doi:10.1016/j.fusengdes.2021.112795

18 V A Maroni, R D Wolson and G E Staahl, Some preliminary considerations of a molten-salt extraction process to remove tritium from liquid lithium fusion reactor blankets, *Nucl. Technol.* **25** 83 (1975). doi:10.13182/NT75-A24351

19 R Delaporte-Mathurin, E A Hodille, J Mougenot, Y Charles and C Grisolia, Finite element analysis of hydrogen retention in ITER plasma facing components using FESTIM, *Nucl. Mater. Energy* **21** 100709 (2019). doi:10.1016/j.nme.2019.100709

20 G R Longhurst, *TMAP7 User Manual*, Idaho National Laboratory report INEEL/EXT-04-02352 Rev. 2 (2008).

21 S Wiesen *et al*, The new SOLPS-ITER code package, *J. Nucl. Mater.* **463** 480 (2015). doi:10.1016/j.jnucmat.2014.10.012

22 D Reiter, M Baelmans and P B\"orner, The EIRENE and B2-EIRENE codes, *Fusion Sci. Technol.* **47** 172 (2005). doi:10.13182/FST47-172

23 P C Stangeby, *The Plasma Boundary of Magnetic Fusion Devices* (Institute of Physics Publishing, Bristol, 2000).

24 T Eich *et al*, Scaling of the tokamak near the scrape-off layer H-mode power width and implications for ITER, *Nucl. Fusion* **53** 093031 (2013). doi:10.1088/0029-5515/53/9/093031

25 A J Creely *et al*, Overview of the SPARC tokamak, *J. Plasma Phys.* **86** 865860502 (2020). doi:10.1017/S0022377820001257

26 M E Austin *et al*, Achievement of reactor-relevant performance in negative triangularity shape in the DIII-D tokamak, *Phys. Rev. Lett.* **122** 115001 (2019). doi:10.1103/PhysRevLett.122.115001

27 A Marinoni, O Sauter and S Coda, A brief history of negative triangularity tokamak plasmas, *Rev. Mod. Plasma Phys.* **5** 6 (2021). doi:10.1007/s41614-021-00054-0

28 P I Ford, *Kronos Physics De-Risking Register*, Kronos Fusion Energy 2026 series. doi:10.5281/zenodo.22133057

29 P I Ford, *A divertor-exhaust concept down-select for a compact spherical-tokamak breeder: Super-X, snowflake, X-point-target, and liquid-metal geometries ranked by peak heat flux and detachment window*, Kronos Fusion Energy 2026 series. doi:10.5281/zenodo.22645933; official page.

30 P I Ford, *A stacked detachment portfolio for a compact spherical-tokamak breeder: Super-X, double-null and snowflake geometries that cut the required argon seed fraction*, Kronos Fusion Energy 2026 series. doi:10.5281/zenodo.22645742; official page.

31 P I Ford, *Real-time detachment control for a Super-X divertor in a compact spherical-tokamak breeder: radiated-power-fraction regulation with a radiative-collapse guard*, Kronos Fusion Energy 2026 series. doi:10.5281/zenodo.22645874; official page.

32 P I Ford, *The negative-triangularity edge: heat-flux width, the ELM-free pedestal, and the scrape-off-layer boundary condition for power handling in a compact spherical-tokamak breeder*, Kronos Fusion Energy 2026 series. doi:10.5281/zenodo.22645830; official page.

33 P I Ford, *Blanket and divertor thermal-hydraulics for a compact spherical-tokamak breeder: coolant heat removal, peak-temperature margins, and the walk-away safety case*, Kronos Fusion Energy 2026 series. doi:10.5281/zenodo.22645836; official page.

34 P I Ford, *Tritium permeation-barrier coatings for a compact spherical-tokamak breeder: the liquid-lithium-over-tin wall-chemistry choice*, Kronos Fusion Energy 2026 series. doi:10.5281/zenodo.22645870; official page.

35 P I Ford, *A real-time tritium-accountancy twin for a compact spherical-tokamak breeder: in-vessel inventory, retention, and self-sufficiency bookkeeping*, Kronos Fusion Energy 2026 series. doi:10.5281/zenodo.22645876; official page.

COLOPHON

How this document was made

The Kronos Fleet — Combined Editorial, 2026 is set in **Fraunces** (display), **Gelasio** (text), and **IBM Plex Mono** (data & equations), carried forward from the Kronos editorial design system.

The figures are rendered at 300 dpi from the deposited generator scripts; the document is composed as a single self-contained file with embedded fonts and imagery, paginated to US Letter, and rendered to PDF through a headless Chromium engine in matched light and dark editions.

Every headline quantity carries an evidence class; withdrawn and restated values are marked as such. Nothing herein is frozen beyond the founder-approved Tier-A set.

Explore it live — turn the interactive 3-D model, run the deposited solvers in the physics validator, and watch the companion film series.

◆

LEGAL NOTICE

Notice, status, and distribution

Conceptual design & simulation study. This document reports a conceptual design and simulation study. It is not a construction commitment, a safety-analysis report, a regulatory filing, or an offer of securities. Forward-looking statements — schedules, costs, market sizes, and performance — are estimates subject to the limitations set out in the Simulations part and may change.

Numbers and their classes. Quantities are reported with evidence classes and case labels; modelled, assumed, and requirement-class values are identified as such and are not to be quoted without their labels.

Public edition. This edition carries the physics and design only; all financial, funding, and defense-commercial content has been removed for public distribution. The scientific text corresponds to the arXiv and journal submissions.

THE 2026 KRONOS SERIES

One programme, many papers

This editorial is one paper in the Kronos 2026 series — a real fusion company's complete, reproducible physics record for a spherical-tokamak breeder and its low-neutron D–^{3}He tandem-mirror burners. Every headline number is a frozen anchor in the Physics De-Risking Register.

Explore the whole programme: the De-Risking Register, the interactive 3-D model, and the physics validator.

KRONOS FUSION ENERGY

A Flowing-Lithium Vapor-Box Divertor with Molten-Salt In-Loop Tritium Extraction for a Compact Spherical-Tokamak Breeder

A real fusion company building real machines. Explore the science, live.

Zenodo · doi:10.5281/zenodo.22645750

Read on kronosfusionenergy.com

The Physics De-Risking Register